NJC

ROYAL SOCIETY OF CHEMISTRY

PAPER

View Article Online
View Journal | View Issue

Cite this: *New J. Chem.*, 2025, **49**, 3464

Understanding the catalytic properties for synthesizing NO_x derivative NH_3 by an alternate gas-switching process†

Ryutaro Wakabayashi, ‡ Yuxiao Zhang,‡ Atsuko Tomita and Tatsuo Kimura *

Received 24th December 2024,
Accepted 31st January 2025

DOI: 10.1039/d4nj05459h

rsc.li/njc

Reactive nitrogen compounds like NO_x are not environment-friendly but have potential as some of the chemical sources for the low-energy synthesis of NH_3 and value-added chemicals. Our recent initiatives have revealed catalytic conversion to NH_3 *via* a gas-switching NO_x storage and reduction process. This concept was demonstrated absolutely by using nanocomposite catalysts based on mesoporous metal oxides with noble metal catalysts and NO_x storage components like BaO/Pt@mAl_2O_3 and BaO/Pt@mTiO_2. Here, we investigate and compare the properties of another BaO/Pt@mCeO_2-type nanocomposite catalyst. After stabilization by zirconium doping, BaO/Pt@m$Ce_{0.8}Zr_{0.2}O_2$ exhibited acceptable NO_x storage properties at temperatures higher than 250 °C with extra NO_x storage by the CeO_2-based support in addition to the major capacity of BaO. However, Pt nanoparticles were made to be very fine by a strong metal–support interaction to CeO_2 and possibly worked very well, which was not preferable for the formation of NH_3. From this viewpoint, the hydrogenation property was suppressed by lowering the reaction temperature, leading to an improvement in the NH_3 selectivity from less than 10% to more than 70% even in the low NO_x storage state.

1. Introduction

Various recycling processes of nitrogen compounds, such as nitrogen oxides (NO_x) and nitrate (NO_3^-), as ammonia (NH_3) have been investigated for overcoming issues with the environment, energy and resources.[1–3] This approach is quite promising for the design of a nitrogen circular economy, where NH_3 is used to obtain value-added organonitrogen compounds like amines.[4–7] Accordingly, the reaction converting harmful NO_x to valuable NH_3 (named as the NTA reaction) is worth investigating through the rational design of heterogeneous catalysts showing high NH_3 selectivity. As one of the interesting approaches, the NO_x storage reduction, NSR, process has been applied by using nanocomposite catalysts, *e.g.*, BaO/Pt/γ-Al_2O_3, for the selective synthesis of NH_3.[8–10] The chemical composition of the catalysts is similar to that developed for the purification to nitrogen (N_2) by NSR.[11–13] In the NTA reaction by modified NSR, the use of hydrogen (H_2) is the standard process for the reduction of NO_x to NH_3.[14,15] From this viewpoint, the chemical composition of the catalysts, such as metal oxide supports and novel metal catalysts, should be investigated further for understanding the catalytic properties. The oxidation of NO, the storage of NO_2, the activation of H_2 and the hydrogenation of the stored NO_3^- proceeded sequentially as the major reactions.

Fundamental study progressed through the use of well-designed nanocomposite catalysts (*e.g.*, BaO/Pt@mAl_2O_3 and BaO/Pt@mTiO_2) for understanding the properties arising from typical components.[16,17] Metal oxide supports such as alumina (Al_2O_3) and titania (TiO_2) were surveyed by combining barium oxide (BaO) and calcium oxide (CaO) as the NO_x storage components and platinum (Pt) as the metal catalyst for activating oxygen (O_2) and H_2. After learning about common NSR catalysts for the purification of NO_x to N_2 in the lean-burn gasoline engine system of automobiles, we proposed a gas-switching NSR process for the synthesis of NH_3 as a game changing technology.[14–17] By modifying the NSR process as a completely different process for the recycling of NO_x, a selectivity towards NH_3 of up to 90% or more was reached in a flow of 5% H_2 by using BaO/Pt@mAl_2O_3 at around 250 °C and CaO/Pt@mAl_2O_3 at around 300 °C.[16] Due to the surface property of the metal oxide support, which supply dissociated hydrogen species, the selectivity of NH_3 was almost maintained in a flow of 1% H_2 by using BaO/Pt@mTiO_2 even at a low temperature (*e.g.*, 175 °C).[17] In this study, for further understanding the significance of the metal oxide support for our gas-switching NSR process for the selective synthesis of NH_3, an additional

National Institute of Advanced Industrial Science and Technology (AIST), Sakurazaka, Moriyama-ku, Nagoya 463-8560, Japan. E-mail: t-kimura@aist.go.jp

† Electronic supplementary information (ESI) available. See DOI: https://doi.org/10.1039/d4nj05459h

‡ These authors equally contributed to this research.

nanocomposite catalyst (*e.g.*, BaO/Pt@mCeO_2) was prepared in the same way using mesoporous ceria (mCeO_2) and compared to BaO/Pt@mAl_2O_3 and BaO/Pt@mTiO_2.

2. Experimental

2.1. Chemicals

Cerium nitrate hexahydrate ($Ce(NO_3)_3{\cdot}6H_2O$), zirconyl nitrate dihydrate ($ZrO(NO_3)_2{\cdot}2H_2O$) and citric acid ($C(OH)(CH_2COOH)_2$-COOH) were obtained from FUJIFILM Wako Pure Chemical Co. Hydrogen hexachloroplatinate(IV) hexahydrate ($H_2PtCl_6{\cdot}6H_2O$) aqueous solution was purchased from Tanaka Precious Metals. Pluronic P123 ($EO_{20}PO_{70}PO_{20}$), as one of the commercial poly(ethylene oxide)-*block*-poly(propylene oxide)-*block*-poly(ethylene oxide) ($EO_nPO_mEO_n$) triblock copolymers, was purchased from Sigma-Aldrich. Barium acetate ($Ba(CH_3COO)_2$) was also obtained from FUJIFILM Wako Pure Chemical Co.

2.2. Synthesis of BaO/Pt@m$Ce_{0.8}Zr_{0.2}O_2$

The Pluronic P123-templated mesoporous structure of pure CeO_2 was not stable and was improved by mixing an appropriate amount of zirconia (ZrO_2). $Ce(NO_3)_3{\cdot}6H_2O$ (4 mmol, 17.4 g), $ZrO(NO_3)_2{\cdot}2H_2O$ (1 mmol, 2.7 g) and citric acid (10 mmol, 19.2 g) were dissolved in an aqueous solution of Pluronic P123 (5 g in 120 mL H_2O) and stirred for 90 min. After combining with another aqueous solution of $H_2PtCl_6{\cdot}6H_2O$ (405.5 μL, 200 g L^{-1} Pt) and stirring for another 30 min, the resultant precursor solution was solidified by using a spray dryer (Yamato Scientific Co., Ltd., ADL311S-A). The inlet temperature and the blower rate were 170 °C and 1.0 m^3 min^{-1}, respectively. After calcination at 400 °C (heating rate; 2 °C min^{-1}) for 3 h in a flow of dry air, Pt@m$Ce_{0.8}Zr_{0.2}O_2$ (1.01 g) was dispersed in H_2O (20 mL), followed by the dropwise addition of an aqueous solution of $Ba(CH_3COO)_2$ (5 mL containing 0.1 g of Ba) under stirring for 1 h and recovered by using a rotary evaporator at 60 °C under vacuum. The weight ratio of Ba : Pt : $Ce_{0.8}Zr_{0.2}O_2$ was 10 : 1 : 100. The resultant powder sample was finally calcined at 500 °C (10 °C min^{-1}) for 3 h in a flow of dry air.

2.3. Characterization of BaO/Pt@m$Ce_{0.8}Zr_{0.2}O_2$

Low- and wide-angle X-ray diffraction (XRD) patterns were recorded by using a Rigaku RINT 2100 with monochromated Fe Kα radiation and a Rigaku RINT 2000 with monochromated Cu Kα radiation, respectively. N_2 adsorption–desorption isotherms were measured by using an Anton Paar Autosorb-iQ at 77 K after the sample was degassed at 110 °C for 6 h under vacuum. The specific surface area was calculated by the Brunauer–Emmett–Teller (BET) method. The total pore volume was estimated by using the volume of N_2 at P/P_0 = 0.99. The pore size distribution curve was drawn by the Barrett–Joyner–Halenda (BJH) method using the desorption branch. Field-emission scanning electron microscopic (FE-SEM) images were taken by using a HITACHI SU9000, operated at 1.0 kV. Transmission electron microscopy (TEM) images were taken by using an FEI Tecnai Osiris, operated at 200 kV, in high-angle annular dark field scanning TEM (HAADF-STEM) mode to enhance the contrast of Pt nanoparticles (NPs) for obtaining clear elemental mapping by energy dispersive X-ray spectroscopy (EDS).

2.4. Catalytic test using BaO/Pt@m$Ce_{0.8}Zr_{0.2}O_2$

According to our previous study,[16,17] the catalytic properties were investigated through our typical gas-switching process between the storage of NO_x and the reduction of stored NO_x (typically NO_3^-) species. The inlet gas was alternated between 1000 ppm NO with 10% O_2 for 60 min and 1% H_2 for 60 min at temperatures ranging from 300 °C down to 175 °C using a fixed-bed flow reactor. All the flow rates were 100 mL min^{-1} balanced with N_2. During the gas-switching operation, the reactor was purged with N_2 for 5 min after every process. Initially, BaO/Pt@m$Ce_{0.8}Zr_{0.2}O_2$ (approximately 100 mg) was placed on quartz glass wool in a quartz glass tube reactor and pre-treated at 300 °C for 60 min in a flow of 1% H_2. The amount of stored NO_x was evaluated on the basis of total NO_x in the gas phase. The formation of nitrogen compounds (*e.g.*, NO, NO_2, N_2O and NH_3) arising from the hydrogenation of the NO_3^- species was monitored using a Fourier-transform infrared (FT-IR) spectrometer (Nicolet iS20, Thermo Fisher Scientific) equipped with a deuterated triglycine sulfate (TGS) detector and a 2.4 m gas cell (Pike Technologies).

Temperature-programmed reduction (TPR) profiles in a flow of H_2 were measured by using a BELCAT II (Microtrac BEL) equipped with a thermal conductivity detector (TCD). A powder sample (approx. 50 mg) was placed inside a triple-walled quartz tube and pre-treated in a flow of O_2 at 300 °C to oxidize adequately, and then cooled down to 40 °C in a flow of He. TPR measurement was conducted at temperatures ranging from 40 °C to 900 °C with a heating rate of 10 °C min^{-1} in a flow of 4% H_2 (Ar balanced, 30 mL min^{-1}) where the resultant water was trapped during the measurement by using a molecular sieve before introduction into the detector.

3. Results and discussion

High-surface-area metal oxides are very important for designing high-performance heterogeneous catalysts. A huge number of papers have so far demonstrated the synthesis of mesoporous metal oxides by applying a drying process of clear precursor solutions containing soluble metal oxide species and an amphiphilic organic compound. However, it is still not easy to reproduce ordered mesoporous metal oxides in powder forms with the self-assembly of amphiphilic organic molecules. We have therefore developed several aerosol-assisted synthetic methods for obtaining powder samples of mesoporous metal oxides, such as Al_2O_3 and TiO_2.[18–22] However, a wet-impregnation method cannot be applied for preparing Pt-supported catalysts based on $EO_nPO_mEO_n$ (*e.g.*, Pluronic P123)-templated mesoporous metal oxides owing to their lower stability in a highly acidic solution of H_2PtCl_6.[23,24] Accordingly, a series of nanocomposite catalysts have been carefully designed by using such mesoporous metal oxides as the catalyst support, especially those prepared using $EO_nPO_mEO_n$. Alkali earth metal species (*e.g.*, BaO) were impregnated after the direct

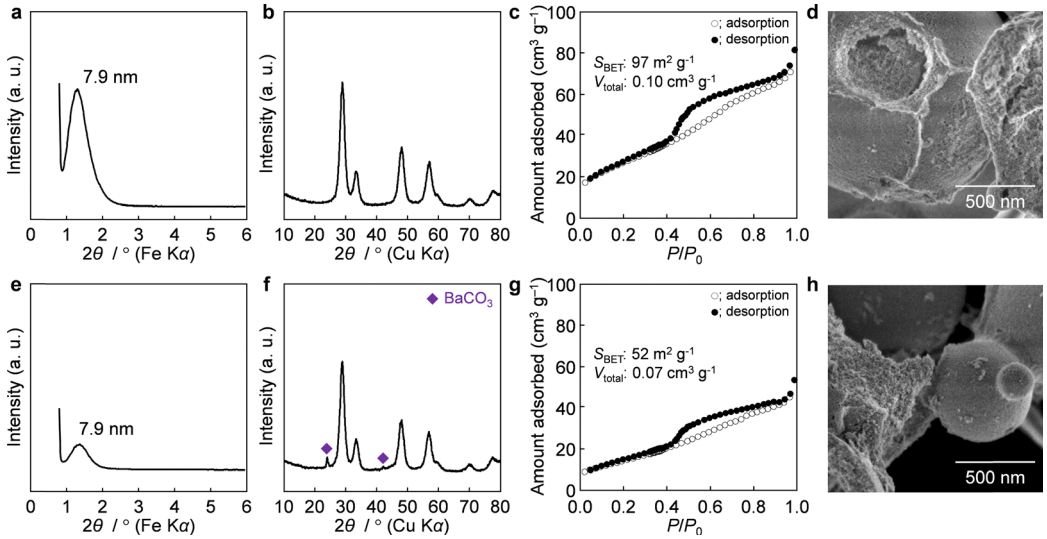

Fig. 1 (a) and (e) Low- and (b), (f) wide-angle XRD patterns, (c) and (g) N_2 adsorption–desorption isotherms and (d), (h) SEM images of (a)–(d) Pt@m$Ce_{0.8}Zr_{0.2}O_2$ calcined at 400 °C for 3 h in dry air and (e)–(h) BaO/Pt@m$Ce_{0.8}Zr_{0.2}O_2$ calcined further at 500 °C for 3 h in dry air.

introduction of the metal catalysts (*e.g.*, Pt) during the spray-drying process. The growth of Pt nanoparticles (NPs) progressed during calcination to remove organic moieties with the crystallization of the metal oxide frameworks. Here, another BaO/Pt@m$Ce_{0.8}Zr_{0.2}O_2$-type nanocomposite catalyst was prepared by the same synthetic process. A Pluronic P123-templated and stabilized mesoporous CeO_2 (mCeO_2)containing Pt species was obtained in one-pot with the preferable addition of ZrO_2 (Pt@m$Ce_{0.8}Zr_{0.2}O_2$). Pt NPs were mainly grown during calcination at 400 °C for 3 h in dry air with the crystallization of CeO_2-based frameworks.

3.1. Structural characterization of Pt@m$Ce_{0.8}Zr_{0.2}O_2$ and BaO/Pt@m$Ce_{0.8}Zr_{0.2}O_2$

Low- and wide-angle XRD patterns, N_2 adsorption–desorption isotherms and SEM images of Pt@m$Ce_{0.8}Zr_{0.2}O_2$ and BaO/Pt@m$Ce_{0.8}Zr_{0.2}O_2$ are shown in Fig. 1. A single dominant peak was observed at $2\theta = 1.4^\circ$ ($d = 7.9$ nm) in the low-angle XRD pattern of Pt@m$Ce_{0.8}Zr_{0.2}O_2$ (Fig. 1a), indicating the presence of a mesostructural ordering derived from the self-assembly of $EO_{20}PO_{70}EO_{20}$ molecules. The wide-angle XRD pattern clearly showed several peaks that can be assigned to the cubic structure of $Ce_xZr_{1-x}O_2$ (Fig. 1b). The peaks were slightly shifted to higher diffraction angles compared to those observed for pure CeO_2 (Table S1, ESI†). For example, the (111) peak was shifted from $2\theta = 28.5^\circ$ to 28.8° without any peak splitting, suggesting the isomorphous substitution of large Ce^{4+} (ionic radius; 0.97 Å) with small Zr^{4+} (0.84 Å).[25] The N_2 adsorption–desorption isotherm was type IV with a hysteresis loop (Fig. 1c), indicating the presence of mesopores. The BET surface area and the total pore volume were 97 $m^2\ g^{-1}$ and 0.10 $cm^3\ g^{-1}$, respectively. The average pore diameter was calculated to be 3.6 nm by the BJH method. A representative SEM image showed partially crushed spherical particles with mesopores (Fig. 1d).

After the impregnation of $Ba(CH_3COO)_2$ followed by calcination at 500 °C for 3 h in a flow of dry air, a modest peak was still observed at almost the same 2θ position in the low-angle XRD pattern (Fig. 1e). This result revealed that the original mesoporous structure of Pt@m$Ce_{0.8}Zr_{0.2}O_2$ was maintained and accommodated the resultant barium species like BaO. As in the case of our previous BaO/Pt@mAl_2O_3 and BaO/Pt@mTiO_2 catalysts,[16,17,23,24] the formation of crystalline BaO species was not confirmed by XRD, but additional peaks were detected at 2θ = 23.9° and 42.0° due to the presence of witherite-type $BaCO_3$ (Fig. 1f).[23] This arises from the thermal decomposition of $Ba(CH_3COO)_2$ to BaO and subsequent reaction with atmospheric CO_2. The N_2 adsorption–desorption isotherm showed a type IV behavior with a hysteresis loop (Fig. 1g). The BET surface area (52 $m^2\ g^{-1}$) and the total pore volume (0.07 $cm^3\ g^{-1}$) decreased with the impregnation of Ba species, which is related to the presence of Ba species inside the mesopores (3.6 nm). A partially crushed spherical porous morphology was also found through SEM observation even after the impregnation of Ba species (Fig. 1h).

Here, spherical mesopores (pore size; 3.6 nm) were designed through the formation of $Ce_{0.8}Zr_{0.2}O_2$-type frameworks with about 1 mass% Pt using a general-purpose spray dryer where the specific surface area and the total pore volume were 97 $m^2\ g^{-1}$ and 0.10 $cm^3\ g^{-1}$, respectively. These values are comparable to those reported in several successful literature studies.[26,27] 2D hexagonal mesoporous $Ce_{0.5}Zr_{0.5}O_2$ (specific surface area; 132 $m^2\ g^{-1}$, pore volume; 0.19 $cm^3\ g^{-1}$ and pore size; 3.7 nm) was prepared by drying a precursor solution containing Pluronic P123, followed by calcination at 400 °C (heating rate; 1 °C min^{-1}).[26] An intense peak was observed at the *d*-spacing of 9.0 nm in the low diffraction angle region after calcination at 400 °C, which deformed with the increase in calcination temperature and almost disappeared after calcination at 600 °C. In another case of $Ce_{0.8}Zr_{0.2}O_2$, the intensity of the corresponding XRD peaks was weakened after calcination at 400 °C where the specific surface area, pore volume and pore size were 107 $m^2\ g^{-1}$, 0.20 $cm^3\ g^{-1}$ and 3.7 nm, respectively. Such 2D hexagonal

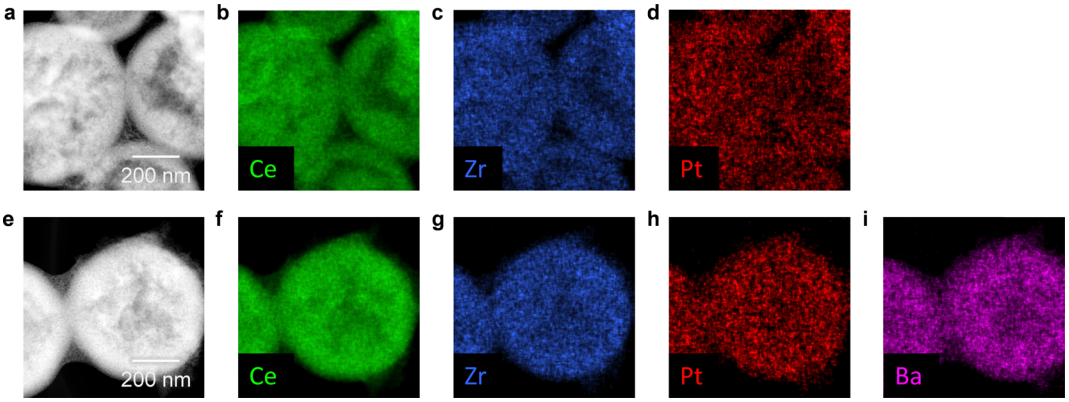

Fig. 2 (a) and (e) HAADF-STEM images and (b)–(d) and (f)—(i) EDS mappings overlapped with Ce, Zr, Pt and/or Ba of (a)–(d) Pt@$mCe_{0.8}Zr_{0.2}O_2$ and (e)–(i) BaO/Pt@$mCe_{0.8}Zr_{0.2}O_2$.

mesoporous $Ce_{0.5}Zr_{0.5}O_2$ (specific surface area; 98 m^2 g^{-1}, pore volume; 0.08 cm^3 g^{-1} and pore size; 4.0 nm after calcination at 400 °C) was reproduced using Pluronic P123.[27] The mesoporous structure can be confirmed by TEM but seemed to deviate (specific surface area; 56 m^2 g^{-1}, pore volume; 0.01 cm^3 g^{-1} and pore size; 7.8 nm).

XRD peaks due to the formation of Pt NPs were not detected in the wide-angle XRD patterns of Pt@$mCe_{0.8}Zr_{0.2}O_2$ after calcination at 400 °C in a flow of dry air (see Fig. 1b) and Ba/Pt@$mCe_{0.8}Zr_{0.2}O_2$ even after calcination at 500 °C (see Fig. 1f). The presence of metallic Pt species is typically confirmed by the presence of the (111) reflection at around 2θ = 40°. The results possibly suggest that the resultant Pt species are extremely fine, being quite different from those observed in our previous case of BaO/Pt@$mTiO_2$ calcined by the same process.[17] The presence of Pt NPs was then surveyed by HAADF-STEM combined with EDS analysis. Typical bright-field TEM observations of Pt@$mCe_{0.8}Zr_{0.2}O_2$ and BaO/Pt@$mCe_{0.8}Zr_{0.2}O_2$ were not successful (see Fig. S1, ESI†) because Ce and Zr are both high atomic number atoms. However, HAADF-STEM, detecting scattered electrons, was quite helpful for illustrating the internal structure at an identical acceleration voltage, revealing a partially hollow morphology of the spray-dried spherical particles (Fig. 2a and e). The presence of Pt NPs was not observed directly by HAADF-STEM, but the EDS spectra suggested the presence of reasonable Pt species (see Fig. S2, ~0.8 mass%, ESI†). The elemental mappings of Ce, Zr, Pt and/or Ba can be illustrated by using the data (Fig. 2b–d and f–i). The resultant size of the Pt NPs is possibly smaller than ~1 nm, under the detection limit by HAADF-STEM. However, the presence of Pt NPs with an average size of around 1 nm was confirmed after the catalytic test (see Fig. S3, ESI†). In addition, a small amount (0.1–0.3 wt%) of chlorine (Cl) was detected for Pt@$Ce_{0.8}Zr_{0.2}O_2$ and Ba/Pt@$Ce_{0.8}Zr_{0.2}O_2$, which arose from the utilization of $H_2PtCl_6 \cdot 6H_2O$ as the Pt source.

3.2. Catalytic properties of BaO/Pt@$mCe_{0.8}Zr_{0.2}O_2$ during the gas-switching NSR process

Catalytic reduction of stored NO_3^- using BaO/Pt@$mCe_{0.8}Zr_{0.2}O_2$ was investigated by an alternate switching of the inlet gas every 60 min between 1000 ppm NO with 10% O_2 and 1% H_2 at temperatures ranging from 300 °C down to 175 °C. As in the case of our recent study,[16,17] Pt NPs were enveloped inside the resultant particles of $mCe_{0.8}Zr_{0.2}O_2$ through the spray-drying of a precursor solution with Pt species followed by calcination at 400 °C. The BaO species were then impregnated using stepwise design to obtain a BaO/Pt@$mCeO_2$ type nanocomposite catalyst for the storage of NO_x and the subsequent hydrogenation to NH_3 and/or N_2. The typical raw data that can be collected under our standard reaction conditions are shown in Fig. 3. The formation of NH_3 was favorable at lower temperatures (*e.g.*, 200 °C and lower). Before starting the reaction process, the electric state of CeO_2 would be initially changed in part from Ce^{4+} to reduced Ce^{3+} in addition to the reduction of Pt NPs to metallic Pt(0) by pretreatment at 300 °C for 60 min in a flow of H_2. In the gas-switching process, it is rational to consider that Ce^{3+} was oxidized to Ce^{4+} during the storage process in a flow of 1000 ppm NO with 10% O_2 and reduced again to Ce^{3+} during the reduction process in 1% H_2.[28] This kind of NSR process is mainly divided into 4 catalytic reactions such as (1) the oxidation of NO by Pt NPs, (2) the storage of NO_2 with BaO, (3) the activation of H_2 over Pt NPs and (4) the hydrogenation of stored NO_3^-. The reaction steps utilizing BaO/Pt@$mCe_{0.8}Zr_{0.2}O_2$ were assessed one-by-one to understand the role of the CeO_2 support and compared to those reported for our BaO/Pt@mAl_2O_3 and BaO/Pt@$mTiO_2$-type catalysts.

The NO oxidation activity over BaO/Pt@$mCe_{0.8}Zr_{0.2}O_2$ in a flow of 1000 ppm NO with 10% O_2 is summarized in Fig. 4, showing the gradual increase with an increase in the reaction temperature. In a previous study on a similar NSR process using common Pt/BaO/CeO_2 (500 ppm NO with 5% O_2 ↔ 5% H_2), the steady-state conversion of NO to NO_2 was increased up to 300 °C and saturated at the equilibrium (*e.g.*, 400 °C).[29] However, the NO oxidation property of BaO/Pt@$mCe_{0.8}Zr_{0.2}O_2$ was not sufficient even at higher temperature (*e.g.*, 250 °C and 300 °C). Additionally, the amount of NO_x, mainly stored as NO_3^- with BaO, is quantified in Fig. 5 at each temperature. This reaction step can be progressed even in a continuous flow of NO_2 as the minor component after a little oxidation of NO by O_2. The storage of NO_x reached up to 0.58 mmol g^{-1} for 60 min

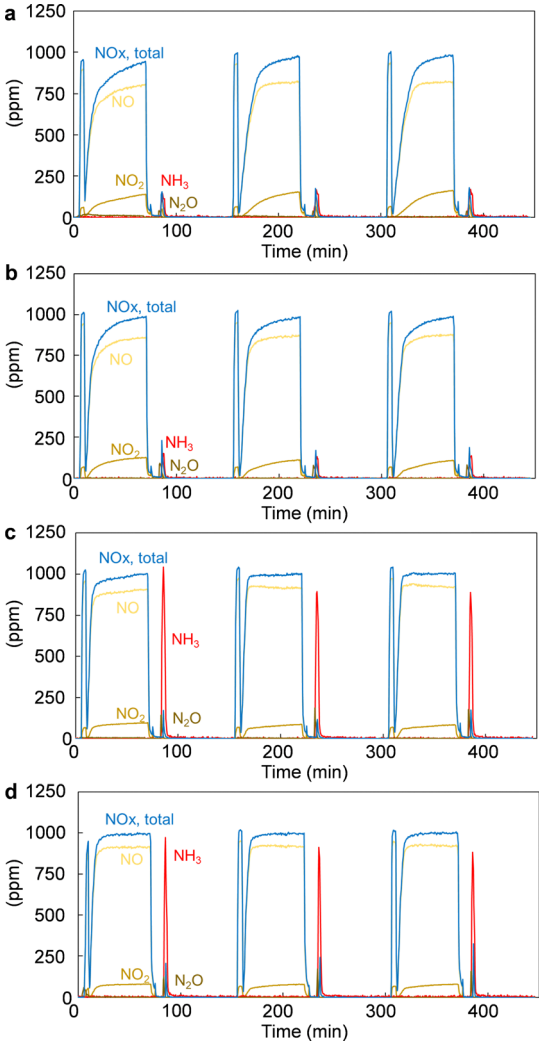

Fig. 3 Time-course plots of nitrogen compounds (*e.g.*, NO, NO_2, N_2O and NH_3) during the alternate gas-switching operation of the inlet gas between 1000 ppm NO with 10% O_2 and 1% H_2 at (a) 300 °C, (b) 250 °C and (c) 200 °C, and down to (d) 175 °C.

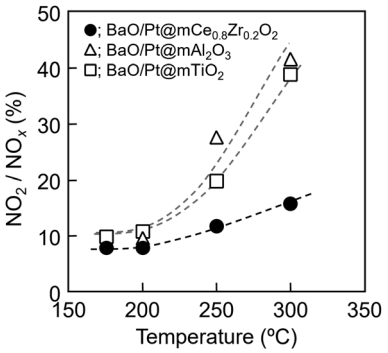

Fig. 4 Temperature-dependence of the NO oxidation property, calculated as the ratio of NO_2/(NO + NO_2) at the end of the 3rd NO_x storage process.

after the 3rd cycle at 300 °C, being superior to those observed for our BaO/Pt@mAl_2O_3 (~0.5 mmol g^{-1}) and BaO/Pt@$mTiO_2$ (~0.2 mmol g^{-1} at 300 °C and 0.26 mmol g^{-1} at 250 °C at the maximum).[16,17] This is very reasonable because CeO_2 can work as an additional NO_x storage component in addition to BaO.[30,31] The amount of stored NO_x was also abundant even at 250 °C (*e.g.*, 0.43 mmol g^{-1}) but drastically decreased at around 200 °C (0.20 mmol g^{-1}) or lower (0.20 mmol g^{-1} at 175 °C). This tendency for the storage of NO_x was not noticeable in our cases using BaO/Pt@mAl_2O_3 and BaO/Pt@$mTiO_2$-type catalysts.

The amount of resultant NH_3 during the reduction process in a flow of 1% H_2 is also displayed in Fig. 5. The slight formation of N_2O was confirmed at the beginning of the reduction process, being similar to the case using BaO/Pt@$mTiO_2$.[17] After the activation of H_2 and subsequent hydrogenation of the stored NO_x, the recovery of NH_3 was very low at temperatures higher than 250 °C (~0.05 mmol g^{-1}), where the formation rate of NH_3 was below 10%. This reaction step was promoted at lower temperatures (0.13 mmol g^{-1} at 200 °C and 0.12 mmol g^{-1} at 175 °C) with ~70% selectivity of NH_3. This behavior is mainly caused by the presence of fine Pt NPs smaller than those grown in mAl_2O_3 (~21 nm as the average) and $mTiO_2$ (~11 nm as the average).[16,17] As observed by HAADF-STEM of BaO/Pt@$mCe_{0.8}Zr_{0.2}O_2$ (see Fig. 2), the hydrogenation of the stored NO_x was accelerated by the presence of extremely fine Pt NPs (smaller than 1 nm). In the case using CeO_2, further oxidation of the resultant NH_3 to N_2 is an extra issue at around 300 °C in the presence of oxidated CeO_2 and thus suppressed below 200 °C.[32,33]

The average size of the resultant Pt NPs is changed with the synthetic process, typically the calcination temperature. Metallic Pt species are dispersed over the surfaces of metal oxides depending on the relationship between the strength of interaction and the amount of interactive sites. For example, Pt interacts strongly with unsaturated penta-coordinated Al^{3+} species (Al_{penta}^{3+}) and is then anchored over the γ-Al_2O_3 surface.[34] Electronic defects are designed at the surfaces of reducible metal oxides (*e.g.*, CeO_2 and TiO_2), leading to strong metal–support interaction (abbreviated as SMSI).[35,36] From this viewpoint, the resultant size of the Pt NPs in Pt@$mCeO_2$ (less than 1 nm, calcined at 400 °C) was very reasonable, being smaller than those observed for Pt@$mTiO_2$ (ave. 11 nm, calcined at 400 °C) and much smaller than those observed for Pt@mAl_2O_3 (ave. 21 nm, calcined at 850 °C). The hydrogenation was completed very quickly in the presence of highly active smaller Pt NPs preferable for the formation of N_2. Accordingly, lower temperature is very suitable for the selective synthesis of NH_3 (~70% at 200 °C, smaller than the ~90% observed for BaO/Pt@$mTiO_2$ at 175 °C).[17]

This consideration was supported by TPR measurements in a flow of H_2. As shown in Fig. 6, a major peak was observed for Pt@$mCe_{0.8}Zr_{0.2}O_2$ at around 250 °C (starting at around 200 °C) and shifted to higher temperature in the presence of Ba species (around 300 °C, starting at around 250 °C). This peak is assignable to the reduction of PtO to Pt, which is promoted with the surface reduction of CeO_2.[28] This variation is due to

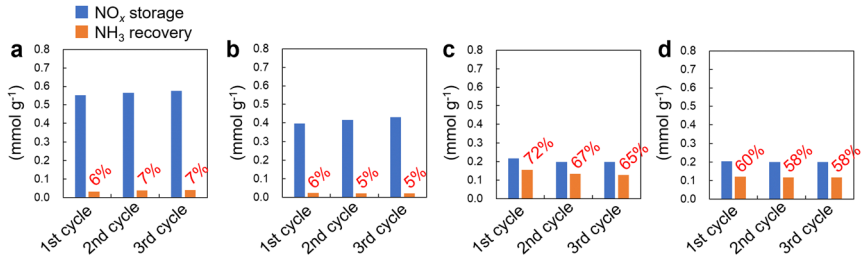

Fig. 5 The amount of stored NO_x in a flow of 1000 ppm NO with 10% O_2 and subsequent formation of NH_3 in a flow of 1% H_2 by using BaO/Pt@m$Ce_{0.8}Zr_{0.2}O_2$ at (a) 300 °C, (b) 250 °C, (c) 200 °C and (d) 175 °C.

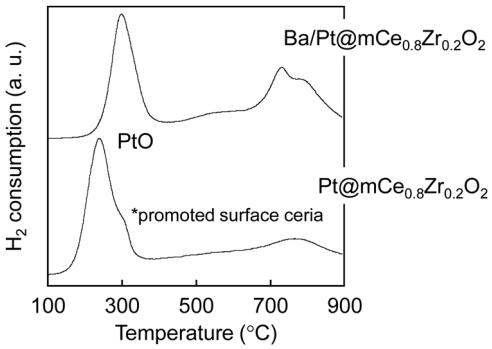

Fig. 6 TPR profiles of Pt@m$Ce_{0.8}Zr_{0.2}O_2$ and BaO/Pt@m$Ce_{0.8}Zr_{0.2}O_2$.

the decrease of accessible Pt surfaces with the coverage through the impregnation of the Ba species. Additionally, the reduction temperature (around 250 °C, starting at around 200 °C) is higher than the case using common Pt/$Ce_{0.25}Zr_{0.75}O_2$ that was prepared by impregnating the same 1.0 wt% Pt and comparable to that observed for $Ce_{0.25}Zr_{0.75}O_2$ having very low Pt (0.001 wt%).[37] It would be better to consider that some of the Pt NPs smaller than 1 nm are possibly embedded inside the framework of $Ce_{0.8}Zr_{0.2}O_2$ with a decrease in the NO oxidation property. As a specific feature of the CeO_2-based catalyst support, a possible formation route of NH_3 by using BaO/Pt@m$Ce_{0.8}Zr_{0.2}O_2$ is illustrated in Fig. 7. During the gas-switching NTA process by the storage of NO_x through the oxidation of NO and subsequent reduction by H_2, lower temperature (*e.g.*, 200 °C and lower) is eventually suitable for the high recovery of NH_3 (improved up to ~70% NH_3 selectivity).

4. Conclusions

The general properties of a BaO/Pt@mCeO_2-type nanocomposite catalyst, specifically those of BaO/Pt@m$Ce_{0.8}Zr_{0.2}O_2$, were investigated for the synthesis of NH_3 through an alternate switching of the inlet gas between 1000 ppm NO with 10% O_2 and 1% H_2 at temperatures below 300 °C. Considering the major components for the catalytic conversion of NO_x in high-temperature combustion gas, we have designed several nanocomposite catalysts, including BaO/Pt@m$Ce_{0.8}Zr_{0.2}O_2$. The resultant size of the Pt NPs was predominantly determined by the synthetic conditions, mainly the calcination temperature. Furthermore, SMSI was very significant for the formation of fine Pt NPs. As a result, the resultant fine Pt NPs (smaller than 1 nm for fresh BaO/Pt@m$Ce_{0.8}Zr_{0.2}O_2$), were highly active as a catalyst, but not fully accessible. Accordingly, high temperature is suitable for the oxidation of NO and subsequent storage as NO_3^- by extra CeO_2 in addition to BaO. For the synthesis of NH_3 by the hydrogenation of stored NO_x species after the activation of H_2, rapid hydrogenation is not suitable for the formation of NH_3.[16,17] This is the main reason that lower reaction temperature is preferable for the high recovery of NH_3. In addition, due to the specific features of CeO_2, like the oxygen storage properties, the oxidation of NH_3 as well as the consumption of H_2 should be suppressed by lowering the reaction temperature,

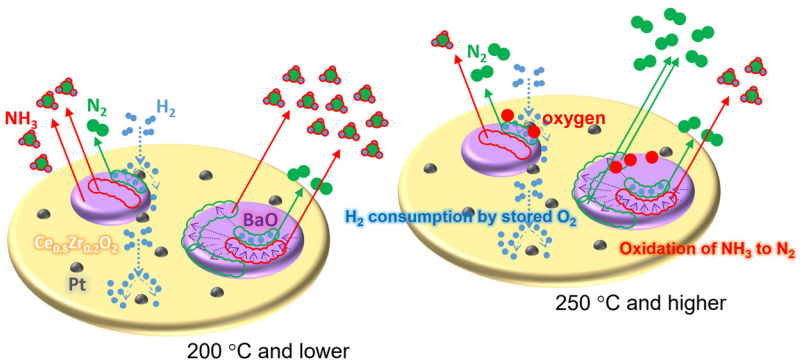

Fig. 7 Possible routes for the formation of NH_3 and N_2 through the reduction of stored NO_x by H_2 utilizing BaO/Pt@m$Ce_{0.8}Zr_{0.2}O_2$.

which allows the oxygen storage properties of the CeO_2-based frameworks to be shown ($\sim$250 °C for BaO/Pt@m$Ce_{0.8}Zr_{0.2}O_2$).

Data availability

Date will be made available on request. Extra data supporting this article are included as a part of the ESI.†

Conflicts of interest

The author declares no competing financial interest.

Acknowledgements

This work has been mainly supported as one of the research projects (JPNP18016, commissioned by the New Energy and Industrial Technology Development Organization, NEDO) in the ''Moonshot R&D program (Moonshot Goal 4: Realization of sustainable resource circulation to recover the global environment by 2050).''

References

1 J. G. Chen, R. M. Crooks, L. C. Seefeldt, K. L. Bren, R. M. Bullock, M. Y. Darensbourg, P. L. Holland, B. Hoffman, M. J. Janik, A. K. Jones, M. G. Kanatzidis, P. King, K. M. Lancaster, S. V. Lymar, P. Pfromm, W. F. Schneider and R. R. Schrock, *Science*, 2018, **360**, eaar6611.
2 M. Nazemi and M. A. El-Sayed, *Acc. Chem. Res.*, 2021, **54**, 4294–4304.
3 Q. Wu, F. Zhu, G. Wallace, X. Yao and J. Chen, *Chem. Soc. Rev.*, 2024, **53**, 557–565.
4 Y. Xiong, Yu Wang, J. Zhou, F. Liu, F. Hao and Z. Fan, *Adv. Mater.*, 2024, **36**, 2304021.
5 P. Liao, J. Kang, R. Xiang, S. Wang and G. Li, *Angew. Chem., Int. Ed.*, 2024, **63**, e202311752.
6 S. Jia, L. Wu, H. Liu, R. Wang, X. Sun and B. Han, *Angew. Chem., Int. Ed.*, 2024, **63**, e202400033.
7 S. R. Udayasurian and T. Li, *Nanoscale*, 2024, **16**, 2805–2819.
8 L. Hollevoet, F. Jardali, Y. Gorbanev, J. Creel, A. Bogaerts and J. A. Martens, *Angew. Chem., Int. Ed.*, 2020, **59**, 23825–23829.
9 L. Hollevoet, E. Vervloessem, Y. Gorbanev, A. Nikiforov, N. De Geyter, A. Bogaerts and J. A. Martens, *ChemSusChem*, 2022, **15**, e202102526.
10 F. V. Steenweghen, L. Hollevoet and J. A. Martens, *Green Chem.*, 2024, **26**, 2534–2539.
11 S. Roy and A. Baiker, *Chem. Rev.*, 2009, **109**, 4054–4091.
12 P. Granger and V. I. Parvulescu, *Chem. Rev.*, 2011, **111**, 3155–3207.
13 J. R. Gonález-Velasco, B. Pereda-Ayo, U. De-La-Torre, M. Urrutxua and R. López-Fonseca, *ChemCatChem*, 2018, **10**, 2928–2940.
14 T. Kimura, *Chem. Rec.*, 2024, **24**, e202400094.
15 T. Kimura, *J. Jpn. Pet. Inst.*, 2024, **67**, 209–216.
16 A. Tomita, R. Wakabayashi and T. Kimura, *Catal. Sci. Technol.*, 2023, **13**, 2927–2936.
17 Y. Zhang, A. Tomita, R. Wakabayashi and T. Kimura, *J. Mater. Chem. A*, 2024, **12**, 8262–8271.
18 H. Maruoka, A. Tomita, Z. Liu and T. Kimura, *Langmuir*, 2018, **34**, 13781–13787.
19 T. Kimura and H. Maruoka, *Chem. Commun.*, 2019, **55**, 10003–10006.
20 H. Maruoka and T. Kimura, *Bull. Chem. Soc. Jpn.*, 2019, **92**, 1859–1866.
21 M. I. Saidul, R. Wakabayashi and T. Kimura, *Dalton Trans.*, 2021, **50**, 7191–7197.
22 Y. Zhang, R. Wakabayashi and T. Kimura, *Dalton Trans.*, 2023, **52**, 1543–1550.
23 R. Wakabayashi, A. Tomita and T. Kimura, *J. Hazardous Mater.*, 2020, **398**, 122791.
24 R. Wakabayashi, A. Tomita and T. Kimura, *Chem. – Eur. J.*, 2021, **27**, 6706–6712.
25 G. Colón, M. Pijolat, F. Valdivieso, H. Vidal, J. Kašpar, E. Finocchio, M. Daturi, C. Binet, J. C. Lavalley, R. T. Baker and S. Bernal, *J. Chem. Soc., Faraday Trans.*, 1998, **94**, 3717–3726.
26 Q. Yuan, Q. Liu, W.-G. Song, W. Feng, W.-L. Pu, L.-D. Sun, Y.-W. Zhang and C.-H. Yan, *J. Am. Chem. Soc.*, 2007, **129**, 6698–6699.
27 L. Xu, H. Song and L. Chou, *Int. J. Hydrogen Energy*, 2012, **37**, 18001–18020.
28 Y. Zhang, Y. Yu and H. He, *Catal. Sci. Technol.*, 2016, **6**, 3950–3962.
29 Y. Ren and M. P. Harold, *ACS Catal.*, 2011, **1**, 969–988.
30 S. Philipp, A. Drochner, J. Kunert, H. Vogel, J. Theis and E. S. Lox, *Top. Catal.*, 2004, **30**, 235–238.
31 A. Filtschew, P. Beato, S. B. Rasmussen and C. Hess, *Phys. Chem. Chem. Phys.*, 2021, **23**, 1874–1887.
32 B. Pereda-Ayo, U. D. L. Torre, M. P. González-Macros and J. R. González-Velasco, *Catal. Today*, 2015, **241**, 133–142.
33 N. L. Phuc, X. Courtois, F. Can, S. Royer, P. Marecot and D. Duprez, *Appl. Catal., B*, 2011, **102**, 362–371.
34 J. H. Kwak, J. Hu, D. Mei, C.-W. Yi, D. H. Kim, C. H. F. Peden, L. F. Allard and J. Szanyi, *Science*, 2009, **325**, 1670–1673.
35 J. Jones, H. Xiong, A. T. DeLaRiva, E. J. Peterson, H. Pham, S. R. Challa, G. Qi, S. Oh, M. H. Wiebenga, X. I. P. Hernández, Y. Wang and A. K. Datye, *Science*, 2016, **353**, 150–154.
36 J. Shan, C. Ye, Y. Jiang, M. Jaroniec, Y. Zheng and S.-Z. Qiao, *Sci. Adv.*, 2022, **8**, eabo0762.
37 N. Kamiuchi, M. Haneda and M. Ozawa, *Catal. Today*, 2014, **232**, 179–184.

